

# Spatial distribution of atypical aftershocks of the 1995 Hyogo-ken Nanbu earthquake

Hiroshi Yamanaka<sup>1</sup>, Yoshihiro Hiramatsu<sup>1</sup>, and Hiroshi Katao<sup>2</sup>

<sup>1</sup>Department of Earth Sciences, Faculty of Science, Kanazawa University, Ishikawa 920-1192, Japan

<sup>2</sup>Research Center for Earthquake Prediction, Disaster Prevention Research Institute, Kyoto University, Kyoto 611-0011, Japan

(Received December 21, 2000; Revised September 24, 2002; Accepted September 26, 2002)

The 1995 Hyogo-ken Nanbu earthquake ( $M_{JMA} 7.3$ ) occurred on January 17, 1995. To reveal the detailed stress field after the mainshock, we relocate hypocenters of aftershocks ( $M \geq 2.3$ ) and determine their focal mechanisms using seismic records obtained by GROUPS-95, a temporary dense seismic network in and around the aftershock region. Along the mainshock rupture zone, some aftershocks are nearly N-S compression or normal fault type events, which is inconsistent with the regional stress field of approximately horizontal E-W compression. We call these aftershocks atypical, defined as events which have focal mechanisms with P-axis directions more than  $45^\circ$  from the regional stress field. The atypical aftershocks amount to about 17% of the total. No temporal variations in aftershock mechanism are found in the analysis period. Their spatial distribution is compared with the slip and stress distribution of the mainshock, as well as the P- and S-wave velocity structure. Most of them are located at the upper boundary between the slipped and unslipped zones of the mainshock. We suggest that the atypical aftershocks are caused by the disturbance of the local tectonic stress field due to the heterogeneous coseismic slip.

## 1. Introduction

The 1995 Hyogo-ken Nanbu earthquake occurred on January 17, 1995 with a magnitude of 7.3 determined by the Japan Meteorological Agency. The hypocenter of the mainshock was located beneath the Akashi Strait in the Kinki District, Japan (Fig. 1). There was severe damage in a wide area, including Kobe city, and more than 6,000 people were killed.

Many aftershocks occurred on the Rokko Fault System, located on the northeastern side of the Akashi Strait, and in the northeastern part of Awaji Island located on the southwestern side of the Akashi Strait, as shown in Fig. 2. The aftershock region extends about 70 km from northeast to southwest (Hirata *et al.*, 1996; Katao *et al.*, 1997). The surface rupture caused by the mainshock was observed along the Nojima Fault which is located on the northwestern coast of Awaji Island (Nakata *et al.*, 1995; Awata *et al.*, 1996). The observation of microearthquake activity for the past 30 years clearly shows that the seismicity along the mainshock rupture zone was low on the southern side of the Arima-Takatsuki Tectonic Line (ATTL) before the mainshock, while the seismicity has been high in the Tamba Plateau on the northern side of ATTL (Katao *et al.*, 1997; Hiramatsu *et al.*, 2000).

The 1995 Hyogo-ken Nanbu earthquake presents many seismologically interesting aspects, including the feature of the aftershock distribution (Hirata *et al.*, 1996; Nakamura and Ando, 1996; Katao *et al.*, 1997), the discrepancy in the fault configuration beneath Akashi Strait (Nakamura and Ando, 1996; Takahashi *et al.*, 1996), the regional stress field after the mainshock (Katao *et al.*, 1997), the slip distribution

of the mainshock (Bouchon *et al.*, 1998; Ide and Takeo, 1997), the stress distribution on the rupture fault before and after the mainshock (Bouchon *et al.*, 1998), the P- and S-wave velocity structure (Zhao and Negishi, 1998), and the S-wave splitting in the aftershock region (Tadokoro *et al.*, 1999).

Comparisons of aftershock distribution with coseismic slip distribution have been done for numerous earthquakes. Mendoza and Hartzell (1988) showed that aftershocks following a large earthquake occur mostly outside of or near the edges of the area of the maximum slip (e.g. 1986 North Palm Springs earthquake, 1983 Borah Peak earthquake). They suggested that slips are continued the outer region of the mainshock rupture area or subsidiary faults are activated.

To investigate the stress field after the Hyogo-ken Nanbu earthquake in and around the mainshock rupture zone, Katao *et al.* (1997) determined the focal mechanisms of aftershocks using permanent seismic networks, and compared them with those of the microearthquakes before the mainshock reported by Iio (1996). Katao *et al.* (1997) reported that some aftershocks showed nearly horizontal N-S or vertical compression axes. Their mechanisms were not consistent with the regional stress field of approximately horizontal E-W compression. Because the stations of the permanent seismic networks were not distributed uniformly over the mainshock rupture, the accuracy of these mechanisms determined was limited.

The Geophysical Research Group Organized by the Universities for Prediction Seismology in 1995 (GROUPS-95) installed 27 temporary seismic stations in and around the aftershock region a week after the mainshock (Hirata *et al.*, 1996) (Fig. 3). Using the seismic records obtained by GROUPS-95, we relocate aftershock hypocenters ( $M \geq 2.3$ ),

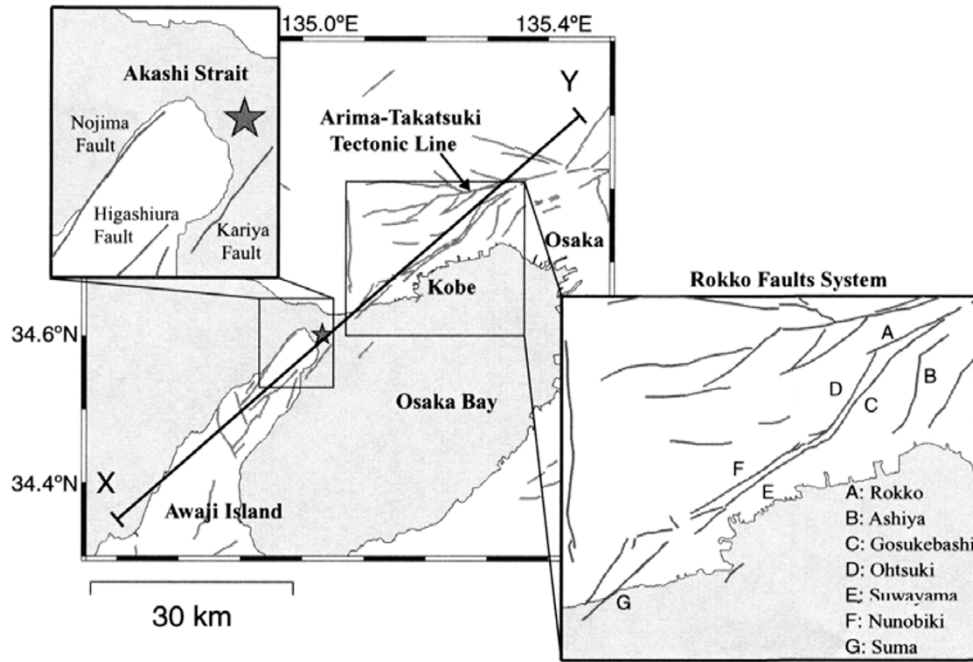


Fig. 1. Distribution of active faults. The Rokko Fault System consists of seven major active faults; (A) Rokko Fault, (B) Ashiya Fault, (C) Gosukebashi Fault, (D) Ohtsuki Fault, (E) Suwayama Fault, (F) Nunobiki Fault and (G) Suma Fault. Line X-Y shows the orientation of the cross section in Figs. 8–11. Star shows the epicenter of the mainshock.

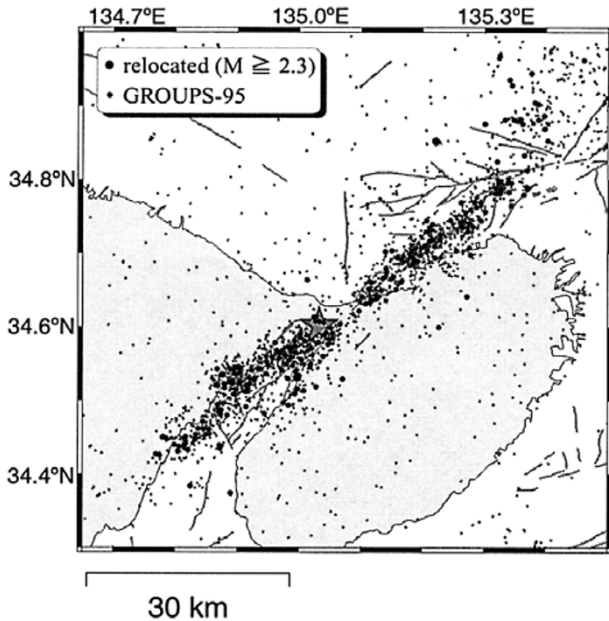


Fig. 2. Distribution of the aftershocks of the 1995 Hyogo-ken Nanbu earthquake. Small dots show the original aftershock locations determined by the GROUPS-95, while solid circles show those ( $M \geq 2.3$ ) relocated in this study.

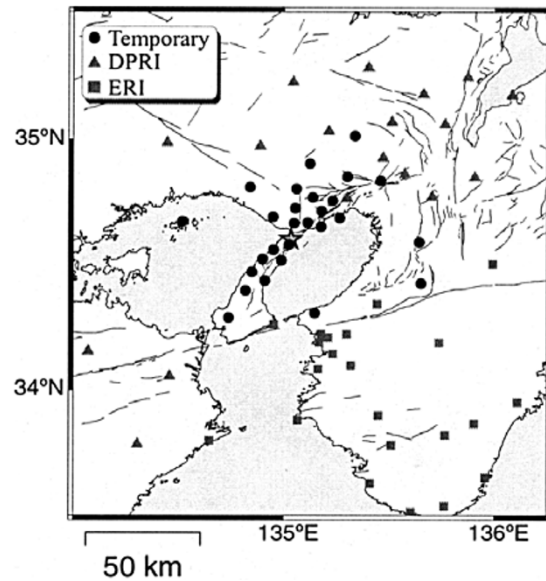


Fig. 3. Distribution of the seismic stations used in this study. Solid circles are the temporary stations deployed by GROUPS-95 after the Hyogo-ken Nanbu earthquake. Gray symbols represent the permanent seismic networks: triangles are the Abuyama, Tottori and Tokushima networks operated by DPRI, Kyoto University, and squares are the Wakayama network operated by ERI, the University of Tokyo. Star shows the epicenter of the mainshock.

and determine their focal mechanisms using P-wave initials. This dense seismic network enables us to determine the locations and focal mechanisms of the aftershocks with a high accuracy. We can also infer the post-seismic stress distribution along the mainshock rupture from these focal mechanisms.

A primary objective of this paper is to describe the characteristics of the spatial distribution of the aftershocks and their focal mechanisms. We compare our results with vari-

ous other geophysical results for the 1995 Hyogo-ken Nanbu earthquake, such as slip and stress distributions and P- and S-wave velocity structures. We show that most of the aftershocks occurred in areas of high stress after the mainshock, while atypical aftershocks, defined later in the discussion section, mainly occurred at the upper boundary of the areas of the maximum coseismic displacement.

Table 1. Focal mechanism solutions of the aftershocks ( $M > 2.3$ ) in the 1st observation period: Time is Japanese Standard Time. The fault parameters follow the notations defined by Aki and Richards (1980). (i.e., Plunge of P-axis and T-axis are measured down from the horizontal.)

No.	Y	M	D	H	M	S	Lat.	Lon.	Dep.	Mag.	Nodal plane - 1			Nodal plane - 2			P - axis		T - axis	
											Strike	Dip	Rake	Strike	Dip	Rake	Plun.	Azim.	Plun.	Azim.
1	95	1	28	16	13	24.34	34.695	135.168	9.00	2.6	270.3	28.8	-36.3	32.7	73.6	-114.0	55.0	272.6	24.9	141.1
2	95	1	28	19	0	27.79	34.613	135.027	15.55	3.2	236.4	65.6	155.7	337.0	68.0	26.4	1.5	106.3	33.9	197.3
3	95	1	28	19	55	11.24	34.613	135.023	15.92	3.4	327.9	23.1	7.1	231.4	87.2	113.0	38.0	300.8	43.2	163.6
4	95	1	29	4	52	36.00	34.384	134.825	8.53	3.0	289.0	72.0	-2.4	19.7	87.8	-161.9	14.3	245.8	11.0	153.0
5	95	1	29	6	8	6.06	34.542	134.937	12.18	2.4	105.2	50.7	-14.1	204.3	79.1	-139.8	35.6	72.7	18.3	328.9
6	95	1	29	9	41	39.05	34.673	135.141	10.13	3.0	57.0	57.6	-151.2	310.6	66.0	-35.9	41.8	270.7	5.3	5.5
7	95	1	29	16	2	45.67	34.695	135.180	8.60	3.3	245.7	75.1	173.4	337.4	83.6	15.0	5.9	110.8	15.1	202.4
8	95	1	30	4	21	54.48	34.707	135.276	11.63	2.7	258.0	49.1	141.3	15.6	61.8	48.0	7.4	134.1	52.8	234.0
9	95	1	30	14	43	36.09	34.543	134.893	2.16	3.2	9.5	58.7	28.6	263.7	65.9	145.3	4.5	318.0	41.1	224.1
10	95	1	30	18	59	14.75	34.519	135.028	10.11	2.6	181.1	32.9	135.9	310.2	67.8	65.1	19.0	58.6	59.4	184.3
11	95	1	31	1	43	20.77	34.545	134.896	0.78	3.2	12.8	18.6	69.9	214.0	72.6	96.6	27.3	298.7	61.9	134.0
12	95	1	31	5	36	49.31	34.699	135.189	10.15	2.4	231.7	59.5	149.2	338.5	63.8	34.4	2.7	104.3	42.1	196.7
13	95	1	31	9	36	6.91	34.734	135.273	5.07	2.7	154.7	46.3	46.3	28.8	58.5	125.9	6.8	94.2	59.1	352.6
14	95	1	31	11	36	32.62	34.539	134.905	2.02	2.6	71.6	49.2	121.0	209.0	49.5	59.2	0.2	320.3	67.0	50.6
15	95	1	31	16	18	52.76	34.944	135.376	7.11	2.4	216.5	60.5	-178.6	125.8	88.8	-29.5	21.3	77.1	19.5	175.0
16	95	1	31	19	34	9.74	34.668	135.153	9.51	2.6	77.6	42.1	-106.5	279.4	50.0	-75.6	78.3	249.5	4.0	359.2
17	95	2	1	1	34	40.25	34.781	135.326	7.68	2.7	61.5	64.5	175.6	153.4	86.0	25.6	14.8	284.6	20.7	20.4
18	95	2	1	5	41	53.98	34.561	134.989	3.79	2.5	200.8	53.3	159.3	303.5	73.5	38.5	12.8	68.1	38.6	168.5
19	95	2	1	12	45	49.05	34.659	135.117	8.01	2.5	304.2	57.5	28.7	197.9	66.1	144.0	5.4	252.8	41.8	158.0
20	95	2	1	18	20	19.47	34.744	135.206	14.90	2.9	354.3	55.8	37.1	241.3	60.1	139.6	2.6	298.7	48.6	205.8
21	95	2	1	21	48	23.92	34.515	134.898	9.62	2.5	246.9	79.3	-175.7	156.1	85.8	-10.7	10.5	111.0	4.6	201.9
22	95	2	1	21	53	55.90	34.541	134.923	6.18	2.7	279.2	40.2	-172.9	183.8	85.5	-50.1	36.6	128.2	29.0	242.5
23	95	2	1	22	51	37.65	34.801	135.338	8.74	2.4	73.0	56.1	178.3	163.9	88.6	33.9	22.1	293.2	24.3	33.8
24	95	2	1	23	30	13.56	34.435	134.872	1.66	2.6	28.6	60.6	177.5	119.8	87.8	29.5	18.7	250.3	22.0	348.2
25	95	2	2	0	15	47.59	34.438	134.874	1.83	2.7	49.6	36.2	178.6	140.7	89.2	53.8	34.1	261.0	35.5	19.9
26	95	2	2	1	52	25.45	34.439	134.871	1.74	2.5	279.2	44.6	-32.8	33.8	67.6	-129.6	50.6	258.6	13.6	151.5
27	95	2	2	2	33	21.56	34.560	134.946	5.40	2.5	281.4	50.3	-157.3	176.5	72.7	-42.0	41.4	131.0	14.0	233.7
28	95	2	2	2	51	3.29	34.455	134.855	10.99	2.8	231.8	58.5	166.8	328.8	78.8	32.2	13.4	96.7	30.5	194.8
29	95	2	2	6	35	12.77	34.736	135.282	6.00	2.5	339.0	64.2	-1.1	69.5	89.0	-154.2	18.7	297.3	17.2	201.3
30	95	2	2	7	39	25.65	34.700	135.187	11.28	2.6	308.6	46.5	11.7	210.4	81.5	135.9	22.5	267.1	36.2	159.4
31	95	2	2	7	39	54.29	34.710	135.203	11.37	2.5	283.0	31.3	-154.7	171.0	77.2	-61.2	49.6	112.7	26.6	238.6
32	95	2	2	9	40	8.60	34.585	135.002	2.81	2.9	353.4	65.7	-2.7	84.5	87.5	-155.6	18.8	311.7	15.1	216.4
33	95	2	2	12	1	57.31	34.854	135.219	9.34	2.5	42.6	22.0	148.6	162.1	78.7	71.0	31.2	267.8	52.5	49.8
34	95	2	2	12	57	22.24	34.701	135.139	5.01	2.7	136.4	40.3	22.1	29.3	75.9	128.2	21.5	91.2	45.3	337.7
35	95	2	2	14	46	30.99	34.511	134.916	10.59	3.1	138.3	33.2	78.4	332.0	57.5	97.5	12.2	56.6	76.2	264.7
36	95	2	2	16	4	19.91	34.589	135.040	5.64	3.6	297.8	24.0	94.3	113.2	66.1	88.1	21.1	204.6	68.8	19.5
37	95	2	2	16	19	27.99	34.703	135.150	17.82	4.5	208.9	45.2	119.6	350.1	51.9	63.6	3.6	98.5	69.2	198.0
38	95	2	2	20	58	2.67	34.732	135.215	11.29	2.9	277.4	40.5	155.2	26.7	74.2	52.2	20.2	144.2	46.9	257.4
39	95	2	2	21	32	21.03	34.707	135.189	10.21	2.5	245.4	67.5	170.1	339.3	80.8	22.8	9.1	110.6	22.5	204.4
40	95	2	2	22	17	29.21	34.480	134.884	4.48	2.5	144.9	68.7	15.0	49.3	76.0	158.0	4.9	98.2	25.3	5.8
41	95	2	3	1	52	9.24	34.790	135.331	7.09	3.5	351.7	82.0	-1.2	81.8	88.8	-172.0	6.5	307.0	4.8	216.5
42	95	2	3	4	36	24.05	34.706	135.188	11.98	3.9	239.2	74.5	-170.3	146.6	80.7	-15.7	17.7	102.2	4.2	193.5
43	95	2	3	14	18	31.59	34.547	134.950	9.11	3.0	279.6	72.6	174.8	11.1	85.0	17.5	8.7	144.1	15.9	236.6
44	95	2	3	20	36	55.61	34.743	135.265	4.09	3.1	340.9	50.9	39.4	223.6	60.5	133.6	5.6	284.2	52.6	186.9
45	95	2	3	21	22	7.11	34.590	135.001	15.71	2.9	226.7	64.8	158.2	326.4	70.3	26.9	3.6	95.6	62.6	187.9
46	95	2	3	23	35	29.47	34.592	135.043	6.52	3.1	94.9	44.5	126.8	228.5	55.8	59.5	6.1	339.7	64.3	82.6
47	95	2	4	0	29	36.18	34.547	134.989	14.85	2.5	307.9	29.9	19.3	201.0	80.5	118.5	29.8	268.2	46.8	140.6
48	95	2	4	1	32	54.85	34.606	135.032	15.60	3.1	342.6	57.9	33.1	233.5	62.5	143.2	2.8	289.0	44.6	196.2
49	95	2	4	12	24	21.64	34.555	135.003	11.46	2.6	73.1	40.7	137.3	198.0	63.7	57.6	12.9	310.9	58.0	62.4
50	95	2	4	16	9	57.69	34.522	134.868	2.74	3.7	252.1	34.9	-147.0	134.0	71.8	-59.7	53.2	80.6	21.0	201.5
51	95	2	4	19	38	0.26	34.523	134.890	12.40	3.7	239.3	83.0	175.9	329.8	85.9	7.0	2.0	104.4	7.8	194.7
52	95	2	5	0	22	7.31	34.557	134.981	8.51	2.6	206.2	71.2	161.9	302.2	72.9	19.7	1.1	73.9	25.8	164.5
53	95	2	5	4	50	-0.70	34.484	134.870	9.09	2.4	21.7	55.7	149.3	130.2	65.1	38.5	5.8	254.0	44.2	349.7
54	95	2	5	6	44	22.69	34.701	135.181	11.53	2.7	22.5	67.2	-170.9	289.0	81.6	-23.1	22.2	243.6	9.8	337.7
55	95	2	5	10	15	0.50	34.691	135.165	10.76	2.6	301.4	76.0	8.4	209.4	81.9	165.9	4.1	255.9	15.7	164.8
56	95	2	5	10	32	8.19	34.527	134.893	13.14	3.5	238.2	26.6	109.5	36.5	65.0	80.5	19.5	133.7	68.6	287.9
57	95	2	5	11	12	10.62	34.678	135.141	9.31	2.4	310.4	56.1	25.4	205.5	69.2	143.4	8.2	260.6	40.2	163.6
58	95	2	5	13	23	39.35	34.692	135.221	10.28	2.4	270.0	42.8	42.5	90.0	47.2	123.6	2.2	180.0	87.8	360.0
59	95	2	5	15	41	24.27	34.517	134.879	6.84	2.4	224.3	60.9	-174.8	131.8	85.4	-29.2	23.6	84.1	16.7	181.7
60	95	2	5	19	46	15.73	34.729	135.208	5.46	2.6	224.9	60.0	-163.4	126.4	75.6	-31.0	31.9	82.0	10.2	178.4
61	95	2	6	3	45	34.44	34.574	134.992	6.01	3.0	212.0	38.3	55.6	73.1	59.3	114.0	11.2	146.0	66.4	29.1
62	95	2	6	13	0	12.76	34.799	135.328	7.26	3.6	244.4	79.2	-176.2	153.7	86.3	-10.9	10.3	108.6	5.0	199.5
63	95	2	6	13	2	4.39	34.798	135.327	7.46	2.4	164.2	51.0	-17.9	265.7	76.2	-139.6	37.8	132.6	16.0	29.7
64	95	2	6																	

Table 1. (continued).

No.	Y	M	D	H	M	S	Lat.	Lon.	Dep.	Mag.	Nodal plane - 1			Nodal plane - 2			P - axis		T - axis	
											Strike	Dip	Rake	Strike	Dip	Rake	Plun.	Azim.	Plun.	Azim.
81	95	2	9	13	19	-0.39	34.531	134.919	14.49	2.7	224.9	78.5	180.0	314.9	90.0	11.5	8.1	89.3	8.1	180.5
82	95	2	9	14	40	25.89	34.525	134.887	9.18	2.8	229.9	65.8	170.7	323.8	81.6	24.5	10.8	94.7	23.2	189.3
83	95	2	9	16	2	15.48	34.451	134.817	1.00	2.8	33.1	74.2	170.9	125.6	81.3	16.0	4.9	258.6	17.5	350.1
84	95	2	10	3	18	36.73	34.779	135.363	2.63	2.9	62.5	67.9	-173.2	329.9	83.7	-22.3	20.1	284.1	10.9	18.1
85	95	2	10	6	39	3.10	34.529	134.996	14.97	2.9	135.7	33.9	69.0	340.6	58.7	103.5	12.7	60.8	72.7	284.5
86	95	2	10	15	19	48.79	34.559	135.039	5.77	3.0	30.9	74.5	170.3	123.5	80.7	15.7	4.3	256.5	17.7	347.9
87	95	2	11	2	25	40.32	34.572	134.982	9.41	2.9	274.6	37.2	145.8	33.0	70.2	57.9	18.9	146.4	53.5	263.8
88	95	2	11	5	20	47.03	34.769	135.262	6.58	2.6	224.8	54.6	168.9	321.2	81.0	35.9	17.4	88.1	31.4	189.1
89	95	2	11	14	29	7.20	34.549	135.018	3.30	2.4	332.8	47.5	61.6	191.4	49.6	117.4	1.1	262.5	69.5	169.5
90	95	2	12	6	11	22.49	34.854	135.220	8.62	2.5	332.9	28.5	86.4	157.0	61.6	92.0	16.6	245.5	73.3	71.8
91	95	2	12	8	24	8.25	34.852	135.220	9.26	2.4	295.3	22.0	43.8	163.7	75.0	106.2	28.2	240.8	57.0	95.0
92	95	2	12	8	31	16.43	34.553	134.947	8.06	2.4	168.6	45.7	7.3	73.5	84.8	135.5	25.5	129.5	33.9	20.9
93	95	2	12	16	25	48.71	34.546	134.902	11.10	2.7	255.0	82.2	177.9	345.3	87.9	7.8	4.1	119.9	7.0	210.4
94	95	2	12	17	48	-0.15	34.717	135.211	10.13	2.5	242.8	58.8	-159.2	141.7	72.3	-32.9	35.5	98.5	8.7	194.8
95	95	2	12	18	4	23.98	34.522	134.892	14.06	3.2	164.4	60.9	-23.8	266.4	69.4	-148.7	36.3	127.8	5.4	33.8
96	95	2	13	5	1	8.81	34.825	135.320	6.08	2.6	200.2	65.4	163.1	297.4	74.7	25.6	6.2	67.3	28.8	160.7
97	95	2	13	10	8	6.62	34.546	135.018	2.63	2.5	184.8	14.3	113.9	340.2	76.9	84.1	31.7	75.1	57.7	242.4
98	95	2	13	20	23	55.45	34.965	135.324	8.43	3.5	214.6	68.9	164.8	310.2	75.8	21.8	4.7	81.4	25.3	173.6
99	95	2	13	20	45	49.74	34.542	134.889	8.98	2.9	238.1	67.5	-174.9	146.2	85.3	-22.6	19.2	99.9	12.3	194.3
100	95	2	14	2	50	49.06	34.531	134.927	14.72	3.1	314.6	78.3	11.3	222.3	78.9	168.0	0.4	268.5	16.3	178.4
101	95	2	14	10	32	45.41	34.735	135.211	11.19	2.7	289.6	48.0	-174.4	195.9	85.8	-42.1	31.6	143.9	24.9	250.5
102	95	2	15	0	3	22.88	34.667	135.138	9.41	2.7	330.2	52.0	36.9	215.3	61.7	135.7	5.7	274.8	50.4	177.8
103	95	2	15	1	3	25.18	34.698	135.178	10.42	2.5	284.6	21.2	-14.1	27.8	84.9	-110.6	46.2	276.8	36.7	135.9
104	95	2	15	1	39	52.56	34.967	135.324	8.92	2.6	307.5	68.1	-14.1	42.9	76.9	-157.5	25.1	266.7	5.9	173.9
105	95	2	15	14	44	27.75	34.508	134.893	9.43	3.3	120.9	41.1	16.5	18.3	79.3	129.9	23.7	78.6	41.7	325.7
106	95	2	15	21	5	44.77	34.447	134.832	3.95	2.7	239.8	48.6	143.1	356.2	63.3	47.8	8.6	114.9	51.8	216.0
107	95	2	15	22	45	39.35	34.548	135.017	2.83	2.7	223.4	16.9	128.3	3.9	76.8	79.3	31.0	102.7	56.9	260.0
108	95	2	16	12	57	19.52	34.694	135.183	8.43	3.1	313.7	66.8	-11.7	48.4	79.2	-156.4	24.2	273.1	8.4	179.3
109	95	2	16	22	25	48.56	34.665	135.136	10.10	2.9	296.2	62.8	21.1	196.2	71.3	151.2	5.5	247.7	33.3	154.0
110	95	2	17	0	10	26.69	34.454	134.850	2.51	2.4	153.6	42.5	114.5	301.9	52.1	69.2	5.0	46.5	73.0	152.9
111	95	2	17	3	9	33.19	34.436	134.815	2.00	3.1	338.9	41.7	34.2	222.0	68.0	126.4	15.3	286.2	52.4	175.4
112	95	2	17	8	52	0.13	34.739	135.216	7.80	2.4	141.4	41.5	-5.7	235.7	86.2	-131.4	35.2	110.8	28.9	358.0
113	95	2	17	20	13	1.62	34.559	134.979	2.15	2.5	15.1	37.7	64.8	225.8	56.4	108.2	9.7	302.9	71.9	181.2
114	95	2	18	1	41	24.56	34.576	135.046	6.34	2.4	323.8	58.5	150.3	70.4	65.0	35.3	4.1	195.8	42.0	289.5
115	95	2	18	2	0	51.97	34.833	135.364	8.88	2.9	323.5	72.1	-3.1	54.4	87.0	-162.0	14.7	280.0	10.5	167.0
116	95	2	18	5	49	7.49	34.534	134.876	1.66	3.1	136.2	44.0	-88.4	313.9	46.0	-91.6	88.5	175.3	1.0	45.0
117	95	2	18	12	12	45.71	34.692	135.185	7.70	2.6	345.2	42.3	28.7	233.1	71.1	128.6	17.1	295.6	48.7	185.1
118	95	2	18	19	29	28.96	34.607	135.026	15.55	2.8	340.9	61.8	24.8	238.6	68.3	149.4	4.2	291.0	36.5	197.9
119	95	2	18	21	1	4.90	34.793	135.330	8.18	2.4	173.9	61.5	21.1	73.5	71.6	149.8	6.6	125.5	34.1	31.0
120	95	2	18	21	37	33.87	34.431	134.804	12.88	3.9	145.2	72.0	-2.6	236.0	87.6	-162.0	14.4	102.0	10.9	9.2
121	95	2	18	23	16	14.66	34.734	135.272	5.15	2.5	350.6	34.0	71.2	192.9	58.0	102.2	12.2	274.1	73.9	135.5
122	95	2	19	1	19	6.39	34.439	134.814	11.55	3.0	141.4	77.2	-10.1	233.6	80.2	-167.0	16.1	97.8	2.1	7.2
123	95	2	19	5	51	28.19	34.437	134.806	11.83	3.6	221.6	77.7	-169.3	129.3	79.5	-12.5	16.2	85.3	1.3	175.6
124	95	2	19	7	2	37.41	34.782	135.320	9.22	2.8	69.7	50.4	166.7	168.3	79.8	40.4	19.0	293.0	35.1	37.0
125	95	2	19	20	15	9.00	34.541	134.893	9.12	2.5	217.4	17.7	128.7	357.3	76.3	78.7	30.4	96.5	57.3	252.5
126	95	2	19	20	27	15.71	34.539	134.897	9.06	3.4	151.0	48.9	5.2	57.6	86.1	138.7	24.7	111.8	30.9	5.8
127	95	2	20	5	43	39.95	34.692	135.160	15.89	2.9	214.9	15.9	161.1	323.1	84.9	74.9	38.1	66.7	48.0	217.1
128	95	2	20	14	41	2.02	34.581	135.008	8.30	2.7	147.2	55.7	6.9	53.2	84.3	145.5	19.2	105.1	28.0	4.5
129	95	2	20	19	8	16.16	34.741	135.275	3.99	2.6	29.4	44.6	119.9	170.4	52.5	63.8	4.2	278.7	69.1	19.6
130	95	2	20	19	36	42.26	34.591	135.054	5.94	2.4	39.2	47.1	29.1	288.5	69.2	133.2	13.3	348.7	47.2	243.9
131	95	2	21	3	53	5.03	34.781	135.318	9.01	2.6	148.5	60.5	1.1	58.0	89.0	150.5	19.7	107.2	21.1	9.3
132	95	2	21	6	36	54.69	34.606	135.040	14.91	3.2	334.0	63.9	14.4	237.6	77.1	153.2	8.8	287.9	28.0	193.2
133	95	2	21	7	15	7.60	34.685	135.184	8.02	2.4	343.1	38.2	17.4	239.2	79.3	126.9	25.2	301.3	43.3	185.0
134	95	2	21	12	34	56.80	34.734	135.265	3.92	2.3	164.5	35.8	71.1	7.4	56.4	103.2	10.5	88.0	74.8	315.3
135	95	2	22	5	56	38.59	34.461	134.845	8.53	3.1	245.3	60.8	-175.6	153.2	86.1	-29.3	23.1	105.3	17.3	202.9
136	95	2	22	22	28	12.02	34.797	135.339	8.79	2.8	153.2	90.0	0.0	63.2	90.0	180.0	0.0	288.2	0.0	198.2
137	95	2	24	8	3	48.09	34.718	135.215	11.66	3.1	43.8	42.9	88.3	226.1	47.2	91.6	2.1	315.0	87.6	163.1
138	95	2	24	12	15	53.93	34.796	135.337	8.84	2.7	67.6	79.4	-175.6	336.7	85.7	-10.7	10.6	291.7	4.4	22.6
139	95	2	24	16	41	53.05	34.664	135.149	7.96	2.6	320.0	53.9	-8.0	54.7	83.5	-143.6	29.8	283.8	19.7	181.9
140	95	2	25	4	44	58.41	34.743	135.267	6.32	2.7	11.3	44.5	105.7	169.8	47.5	75.1	1.5	270.3	78.9	8.2
141	95	2	25	12	59	20.69	34.540	134.993	14.93	3.3	142.1	46.1	73.9	344.7	46.2	106.1	0.0	63.4	78.5	333.4
142	95	2	25	14	24	53.36	34.578	134.961	0.82	9.9	26.2	38.1	92.8	202.6	52.0	87.8	6.9	294.2	82.9	100.1
143	95	2	25	16	53	55.64	34.528	134.925	14.37	3.0	234.0	68.5	-165.3	138.5	76.4	-22.2	25.2	94.9	5.3	187.4
144	95	2	27	5																

Table 1. (continued).

No.	Y	M	D	H	M	S	Lat.	Lon.	Dep.	Mag.	Nodal plane - 1			Nodal plane - 2			P - axis		T - axis	
											Strike	Dip	Rake	Strike	Dip	Rake	Plun.	Azim.	Plun.	Azim.
161	95	3	6	19	7	53.10	34.481	134.873	9.63	3.2	126.7	90.0	0.0	36.7	90.0	180.0	0.0	261.7	0.0	171.7
162	95	3	7	16	20	26.25	34.565	134.993	6.14	2.5	64.1	33.5	129.4	199.6	64.7	67.2	16.7	306.2	63.1	72.4
163	95	3	8	3	18	46.31	34.493	134.982	3.92	2.8	206.0	22.2	44.4	73.9	74.7	106.3	27.9	150.9	57.3	5.4
164	95	3	8	3	29	29.49	34.494	134.982	3.76	2.6	190.1	6.5	28.4	71.9	86.9	95.7	41.6	156.4	47.8	347.9
165	95	3	8	20	5	0.55	34.450	134.784	1.54	2.7	246.2	55.2	149.8	354.6	65.6	38.8	6.4	118.3	44.1	214.5
166	95	3	8	23	11	7.02	34.688	135.192	9.28	2.6	39.4	43.1	-133.5	271.8	60.3	-57.2	60.1	232.0	9.5	338.9
167	95	3	9	5	18	36.55	34.881	135.347	1.07	2.4	199.5	66.8	-172.1	106.3	82.7	-23.4	21.6	60.6	10.9	155.0
168	95	3	9	8	35	2.33	34.530	134.925	14.04	2.4	163.7	25.1	50.4	26.1	70.9	106.6	24.2	103.3	60.6	320.4
169	95	3	9	20	32	39.29	34.648	135.133	8.18	3.0	339.3	50.5	-13.5	78.0	79.6	-139.7	35.3	306.7	18.8	202.7
170	95	3	10	0	33	56.65	34.621	135.097	9.51	2.6	318.9	42.7	13.4	219.0	81.0	131.9	24.1	277.8	39.1	166.5
171	95	3	11	9	41	36.34	34.513	135.007	14.19	3.1	301.2	48.9	132.6	66.7	56.3	52.2	4.2	182.5	59.0	279.4
172	95	3	12	0	32	49.06	34.427	134.769	4.36	2.4	333.9	33.4	0.4	243.6	89.8	123.4	36.0	304.8	36.4	182.5
173	95	3	12	20	17	25.41	34.880	135.352	1.61	2.9	184.6	56.5	174.7	277.5	85.6	33.7	19.7	46.2	26.4	146.4
174	95	3	13	7	30	38.11	34.537	134.902	4.39	2.4	344.7	44.6	38.5	225.2	64.1	127.7	11.2	289.1	54.3	183.1
175	95	3	14	1	14	1.19	34.936	135.340	11.55	2.7	18.2	51.5	140.1	135.7	59.8	46.1	4.9	255.2	52.7	351.7
176	95	3	14	20	59	42.55	34.598	135.050	5.64	2.4	227.6	23.9	92.8	44.5	66.2	88.7	21.2	135.4	68.8	312.0
177	95	3	15	10	39	8.44	34.542	134.867	0.84	2.6	3.3	46.8	25.0	255.6	72.0	133.9	15.5	315.0	44.6	209.1
178	95	3	16	9	30	21.14	34.549	134.980	8.28	2.5	198.1	61.4	172.4	291.7	83.3	28.8	14.9	61.6	24.9	158.7
179	95	3	16	13	54	51.35	34.426	134.774	4.82	3.2	200.0	34.6	60.5	54.5	60.4	108.8	13.4	131.0	68.7	3.3
180	95	3	17	10	40	2.24	34.509	134.993	15.58	2.5	150.1	39.2	103.7	312.6	52.2	79.0	6.6	50.4	79.1	177.3
181	95	3	18	14	54	12.20	34.643	135.125	12.22	2.6	65.8	45.0	81.9	257.2	45.6	98.0	0.3	341.5	84.3	248.6
182	95	3	18	20	30	6.06	34.880	135.351	2.22	2.4	302.8	57.5	10.3	207.2	81.3	147.1	15.8	259.1	29.1	160.0
183	95	3	18	23	43	31.93	34.875	135.301	3.78	2.8	152.5	44.1	113.7	301.0	50.4	68.7	3.3	46.0	73.4	146.9
184	95	3	20	20	3	7.98	34.739	135.262	1.87	2.5	218.4	44.7	106.5	15.8	47.5	74.3	1.4	116.9	78.4	213.8
185	95	3	22	18	1	6.51	34.539	134.895	10.16	2.5	246.6	70.2	163.1	342.5	74.1	20.7	2.7	114.0	25.7	205.3
186	95	3	23	0	49	43.95	34.556	134.966	6.60	2.8	214.6	45.3	25.8	105.8	71.9	132.3	16.1	166.1	45.8	58.8
187	95	3	23	7	7	56.98	34.512	134.912	10.45	2.5	126.8	41.3	44.6	0.2	62.4	122.0	11.7	67.7	59.2	317.3
188	95	3	25	0	50	17.71	34.462	134.837	10.13	2.8	64.8	61.6	-147.3	317.8	61.6	-32.7	42.3	281.3	0.0	11.3
189	95	3	25	11	31	15.09	34.887	135.396	11.60	2.4	293.9	29.0	-8.6	31.4	85.8	-118.8	42.0	274.1	34.5	145.8
190	95	3	27	0	30	19.69	34.783	135.340	12.34	2.5	67.4	71.8	-178.8	337.0	88.8	-18.2	13.6	290.7	11.9	23.6
191	95	3	28	7	23	8.29	34.869	135.397	13.11	2.5	37.2	39.1	142.5	158.0	67.4	57.2	16.1	271.5	55.1	25.9
192	95	3	28	11	56	49.18	34.876	135.361	-0.53	2.9	17.8	77.1	167.1	110.7	77.4	13.3	0.3	244.2	18.2	334.3
193	95	3	29	1	14	0.43	34.765	135.343	10.29	2.4	241.7	75.6	172.4	333.6	82.6	14.5	4.9	107.0	15.5	198.4
194	95	3	29	14	57	27.99	34.516	134.917	5.26	2.3	319.1	32.4	28.8	204.1	75.0	119.1	24.4	271.9	51.2	147.5
195	95	3	30	14	42	1.63	34.788	135.319	8.34	2.5	50.0	40.8	139.9	172.6	65.1	56.5	13.7	286.2	56.4	37.8
196	95	3	31	5	10	33.44	34.756	135.301	4.20	2.8	17.7	41.4	66.8	227.4	52.6	109.1	5.8	304.0	73.8	193.5
197	95	4	1	3	53	33.71	34.482	134.943	7.03	2.6	158.7	41.3	44.6	32.2	62.3	122.1	11.7	99.6	59.2	349.3
198	95	4	2	13	28	1.69	34.553	134.983	13.26	2.5	259.7	32.3	119.1	46.3	62.2	72.9	15.6	148.8	68.1	282.5
199	95	4	2	14	33	26.60	34.650	135.157	8.45	3.0	302.4	32.4	20.9	194.6	79.0	120.6	27.5	260.6	47.1	136.5
200	95	4	3	1	45	0.52	34.881	135.333	1.75	2.5	121.7	49.6	13.6	22.8	79.7	138.8	19.4	78.5	35.8	333.8
201	95	4	3	11	14	12.25	34.559	134.987	8.38	2.3	263.6	81.0	7.1	172.5	83.0	170.9	1.4	218.2	11.4	127.9
202	95	4	3	22	31	45.35	34.529	134.926	14.76	2.7	328.4	57.5	18.4	228.2	74.5	146.1	11.0	281.5	34.7	183.8
203	95	4	4	1	36	22.30	34.604	135.066	9.42	2.8	72.7	52.8	145.9	184.9	63.5	42.5	6.4	306.6	48.0	43.7
204	95	4	4	1	39	5.54	34.769	135.294	5.11	2.3	168.9	38.1	99.3	337.1	52.5	82.8	7.3	72.3	80.7	213.6
205	95	4	4	2	50	2.84	34.729	135.273	1.30	2.6	185.9	40.7	106.0	345.2	51.2	76.6	5.3	84.6	78.3	201.4
206	95	4	5	2	12	24.16	34.784	135.327	4.71	2.8	159.6	40.5	-53.0	294.9	58.8	-117.1	64.8	155.7	9.9	44.0
207	95	4	6	10	50	48.62	34.793	135.326	6.41	2.7	82.4	69.5	-158.2	344.5	69.7	-21.9	29.5	303.4	0.1	33.5
208	95	4	6	10	55	4.87	34.790	135.328	6.45	2.6	271.2	73.8	-171.6	178.8	82.0	-16.4	17.2	134.1	5.7	225.9
209	95	4	6	11	0	8.05	34.789	135.329	5.55	2.6	250.0	37.6	-165.0	148.0	80.9	-53.3	42.2	92.8	26.6	209.8
210	95	4	6	20	22	6.03	34.794	135.328	6.62	2.3	260.5	37.2	-172.8	164.8	85.7	-53.0	38.1	107.5	30.6	225.2
211	95	4	7	1	9	31.36	34.523	134.920	6.00	2.9	301.5	36.4	-5.8	36.1	86.6	-126.2	37.7	274.2	31.8	155.6
212	95	4	7	4	34	28.11	34.660	135.165	8.85	2.8	231.0	40.0	103.5	33.6	51.3	78.9	5.7	131.5	79.6	254.6
213	95	4	7	10	8	38.87	34.791	135.325	6.23	2.5	259.1	43.8	-148.4	145.2	68.8	-50.7	50.0	99.3	14.7	207.6
214	95	4	10	21	17	34.23	34.433	134.820	14.14	3.3	171.9	45.3	119.5	313.1	51.8	63.5	3.4	61.5	69.2	160.5
215	95	4	11	7	38	2.19	34.554	134.983	8.79	3.0	280.2	57.5	5.5	187.2	85.4	147.4	18.8	238.2	25.9	138.7
216	95	4	12	13	40	0.57	34.561	134.977	14.38	2.5	130.4	60.6	3.3	38.8	87.1	150.6	18.1	88.4	22.5	350.6
217	95	4	12	23	2	37.74	34.782	135.321	7.79	2.8	157.8	79.4	4.4	67.0	85.7	169.4	4.4	112.8	10.6	22.0
218	95	4	13	5	49	33.59	34.607	135.032	15.53	2.4	240.7	36.0	148.2	357.3	71.9	58.3	20.6	110.7	52.3	229.9
219	95	4	13	22	29	32.01	34.880	135.355	1.59	2.6	305.2	54.2	22.4	201.6	72.0	142.1	11.2	257.0	39.2	157.7
220	95	4	14	16	33	15.27	34.770	135.284	9.53	2.5	230.2	16.3	-175.0	135.4	88.6	-73.7	44.1	61.4	41.4	210.1
221	95	4	15	7	29	42.78	34.531	134.928	3.19	2.3	171.5	21.8	-160.1	63.0	82.7	-69.3	48.2	355.0	34.5	135.4
222	95	4	15	19	26	28.61	34.782	135.326	7.50	2.5	310.8	29.6	-13.6	52.6	83.3	-118.9	44.2	294.2	32.2	166.5
223	95	4	15	19	55	25.41	34.784	135.325	6.96	2.4	310.2	52.2	-35.9	64.1	62.4	-136.3	49.6	282.2	6.0	185.0
224	95	4																		

Table 1. (continued).

No.	Y	M	D	H	M	S	Lat.	Lon.	Dep.	Mag.	Nodal plane - 1			Nodal plane - 2			P - axis		T - axis	
											Strike	Dip	Rake	Strike	Dip	Rake	Plun.	Azim.	Plun.	Azim.
241	95	5	6	1	9	14.28	34.881	135.387	4.55	3.1	31.0	56.1	-153.1	285.2	67.9	-37.0	41.3	243.9	7.4	340.5
242	95	5	6	2	44	7.73	34.516	134.996	10.81	3.1	249.2	46.6	111.0	40.1	47.3	69.3	0.3	144.6	74.9	235.9
243	95	5	8	2	36	13.49	34.703	135.255	11.08	3.5	316.2	43.6	91.7	133.9	46.4	88.4	1.4	225.0	88.2	6.4
244	95	5	11	17	3	29.85	34.709	135.220	11.31	2.5	256.9	80.2	-174.0	165.9	84.1	-9.8	11.1	121.1	2.7	211.6

Table 2. Focal mechanism solutions of the aftershocks ( $M > 2.3$ ) in the 2nd observation period.

No.	Y	M	D	H	M	S	Lat.	Lon.	Dep.	Mag.	Nodal plane - 1			Nodal plane - 2			P - axis		T - axis	
											Strike	Dip	Rake	Strike	Dip	Rake	Plun.	Azim.	Plun.	Azim.
1	95	10	5	4	22	14.84	34.744	135.295	2.24	2.9	172.5	49.6	43.8	50.6	58.2	130.3	4.9	113.3	56.2	15.9
2	95	10	6	13	37	10.57	34.568	135.013	5.05	2.2	174.5	46.4	35.4	58.4	65.2	130.5	11.1	120.5	51.7	16.2
3	95	10	11	11	56	54.86	34.853	135.403	5.57	2.7	67.1	49.4	-170.8	331.1	83.0	-40.9	33.1	280.7	22.0	25.9
4	95	10	13	2	47	53.37	34.962	135.461	12.88	2.3	262.2	60.9	-159.8	162.0	72.4	-30.7	33.9	119.1	7.5	214.2
5	95	10	13	14	41	52.87	34.578	135.031	12.93	2.5	52.4	36.6	104.6	214.4	54.7	79.4	9.2	312.0	77.4	88.1
6	95	10	14	2	4	6.08	34.637	135.116	10.78	4.6	46.7	35.3	69.8	251.0	57.1	103.8	11.1	331.1	73.9	198.3
7	95	10	14	2	5	16.58	34.641	135.129	10.90	3.5	342.3	41.3	26.6	231.7	72.8	128.1	18.8	294.2	47.7	182.2
8	95	10	14	2	39	32.99	34.642	135.124	11.77	2.2	251.8	52.0	129.4	18.7	52.5	50.9	0.2	135.1	60.0	225.6
9	95	10	14	21	27	27.21	34.567	134.985	8.60	2.5	73.2	61.4	-24.3	175.5	68.8	-149.1	36.5	36.5	4.8	303.0
10	95	10	15	1	32	47.67	34.633	135.115	12.15	2.7	199.4	54.1	43.2	80.5	56.3	135.2	1.3	140.4	53.8	48.6
11	95	10	22	1	1	28.93	34.852	135.224	9.77	2.4	299.5	74.7	-10.0	32.2	80.3	-164.5	17.8	256.5	3.8	165.2
12	95	10	23	17	14	34.78	34.725	135.228	6.15	2.4	326.4	55.6	6.5	232.7	84.7	145.4	19.5	284.5	27.7	183.8
13	95	10	25	21	56	50.53	34.637	135.123	11.34	2.3	43.2	32.6	87.9	225.7	57.4	91.4	12.4	314.7	77.6	140.2
14	95	11	9	20	29	52.55	34.454	134.832	8.84	3.2	258.6	52.5	-146.3	146.5	63.9	-42.7	47.9	107.3	6.9	204.9
15	95	11	13	10	56	-0.27	34.570	134.987	7.11	2.6	225.4	48.9	-174.4	131.7	85.7	-41.2	31.1	80.1	24.4	186.0
16	95	11	13	15	30	57.14	34.638	135.125	11.71	2.7	59.5	33.6	118.1	206.9	60.8	72.7	14.1	309.4	69.1	80.7
17	95	11	15	11	55	15.77	34.641	135.101	10.89	2.3	73.2	50.7	130.2	200.0	53.8	51.7	1.7	316.0	59.9	49.0
18	95	11	15	19	58	46.50	34.813	135.369	9.54	2.5	222.9	40.5	157.4	330.4	75.5	51.7	21.2	88.4	45.6	201.7
19	95	11	16	16	23	57.24	34.536	134.946	12.38	2.2	202.8	40.4	103.4	5.5	50.9	78.9	5.4	103.3	79.8	224.8
20	95	11	17	17	46	52.13	34.642	135.124	11.53	2.2	24.7	45.8	33.2	270.2	66.9	130.7	12.5	332.0	50.4	226.5
21	95	11	19	15	42	19.86	34.528	134.927	14.54	2.6	234.3	73.8	-171.6	142.0	82.0	-16.4	17.2	97.2	5.7	189.0
22	95	11	23	17	1	28.03	34.584	135.054	8.20	2.3	149.8	40.0	103.5	312.4	51.3	78.9	5.8	50.3	79.6	173.6
23	95	12	8	17	15	8.57	34.718	135.228	11.50	2.7	175.3	41.4	26.8	64.6	72.6	128.2	18.6	127.1	47.9	15.2
24	95	12	16	4	49	38.44	34.375	134.889	13.44	3.1	95.0	29.7	18.4	348.9	81.0	118.4	30.2	56.0	46.5	288.1
25	95	12	22	19	7	12.05	34.461	134.854	9.16	3.3	147.6	41.6	41.2	24.4	64.1	123.8	12.7	90.7	56.9	340.5
26	95	12	27	9	18	15.17	34.439	134.799	6.17	3.1	145.2	68.8	15.1	49.7	75.9	158.1	4.8	98.5	25.3	6.2
27	96	1	3	20	55	30.24	34.905	135.382	0.69	3.1	294.1	75.7	-11.4	26.9	78.9	-165.5	18.1	250.9	2.2	160.2
28	96	1	4	15	19	56.56	34.795	135.323	13.60	2.3	111.1	45.5	-77.9	274.0	45.8	-102.1	81.4	103.3	0.1	12.5
29	96	1	5	19	29	14.35	34.698	135.278	13.29	2.3	195.4	45.7	131.1	324.1	57.4	56.1	6.5	77.5	61.1	179.4
30	96	1	8	3	37	14.79	34.903	135.387	0.08	2.9	190.4	64.4	176.5	281.9	86.9	25.7	15.5	53.3	20.2	149.2
31	96	1	10	15	57	24.12	34.541	134.972	14.34	2.2	245.4	43.3	81.6	76.9	47.3	97.8	2.0	161.4	83.9	51.8
32	96	1	11	2	5	29.74	34.903	135.387	0.82	2.4	117.2	70.9	-17.8	213.2	73.3	-160.0	25.8	75.6	1.6	344.8
33	96	1	11	2	22	12.65	34.599	135.226	7.63	2.3	193.7	39.3	107.5	351.6	52.9	76.2	6.9	91.4	77.0	213.1
34	96	1	15	7	20	24.48	34.537	134.895	9.95	2.4	215.9	54.8	141.5	330.5	59.4	42.0	2.7	92.3	50.1	185.5

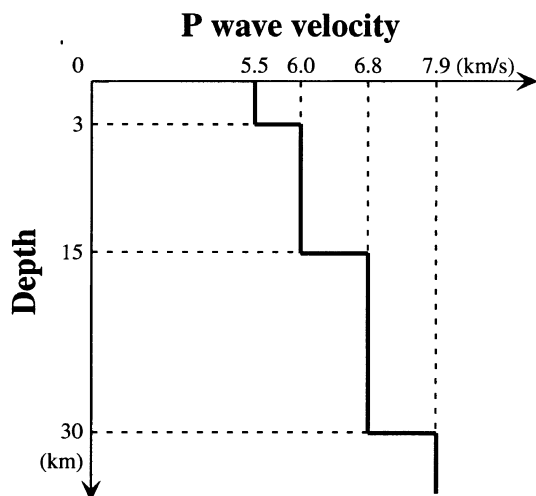


Fig. 4. P-wave velocity structure used for hypocenter determination.

## 2. Data and Method

We relocate the aftershocks with magnitudes greater than 2.3 and determine their focal mechanisms using the data obtained by GROUPS-95. It is hard to determine focal mechanisms of smaller events due to the small number of recorded seismograms and unclear initial motions of P-waves.

GROUPS-95 deployed 27 temporary seismic stations, mainly in the aftershock region, in addition to the permanent regional seismic networks: the Abuyama, Tottori and Tokushima networks operated by the Disaster Prevention Research Institute (DPRI), Kyoto University; and the Wakayama network operated by the Earthquake Research Institute (ERI), University of Tokyo. Temporary stations were operated during two periods; one from January 26, 1995 to May 12, 1995, and the other from October 1, 1995 to January 12, 1996. The installations of the 27 temporary seismic stations were completed on February 14, 1995. We note, however, that the number of the temporary seismic stations was reduced to 10 in April, 1995. For the GROUPS-95 data set, arrival times of P- and S-waves and P-wave polarities were scanned manually after several automatic data processings. However, P-wave polarities and travel times may have

large errors, in particular, for those stations far away from the aftershock area, because a large amount of data was processed quickly in a short time. We therefore reexamined all the P-wave arrival times and polarities for the aftershocks ( $M \geq 2.3$ ) manually using the WIN system (Urabe and Tsukada, 1991). The hypocenters are determined from those re-picked arrival times by using the software HYPOMH (Hirata and Matsu'ura, 1987). The P-wave velocity structure used for the hypocenter determination is shown in Fig. 4. To improve the accuracy of the hypocenter determination, we did not use the data at the stations with epicentral distances greater than 50 km. Further, we discarded data with unclear and/or weak onsets of P-waves due to a low signal-to-noise ratio. From the P-wave polarities rechecked in this study, we determined the focal mechanisms for all the aftershocks with  $M \geq 2.3$ , using the scheme of Maeda (1992). Finally, we obtained the focal mechanisms of 244 and 34 events along the mainshock rupture zone for the first and second periods, respectively. The 95% confidence limits for the obtained P- and T-axis directions are typically  $\pm 5^\circ$  for azimuth and  $\pm 15^\circ$  for plunge.

### 3. Result

Figures 5, 6 and 7 show the locations, focal mechanisms and directions of P-axes of the aftershocks analyzed in this study. Fault parameters of these aftershocks are listed in Table 1 (1st period) and Table 2 (2nd period). Following Katao *et al.* (1997), we classify the focal mechanisms into four types: normal fault with a plunge of the P-axis  $> 60^\circ$ ; reverse fault with a plunge of the T-axis  $> 60^\circ$ ; strike-slip fault with a plunge of the Null-axis  $> 45^\circ$ ; and intermediate type otherwise.

On the basis of the rupture propagation of the mainshock (Ide and Takeo, 1997; Bouchon *et al.*, 1998) and the aftershock activity (Katao *et al.*, 1997), we divide the aftershock zone into three regions: the Kobe region (from the Akashi Strait to the Arima-Takatsuki Tectonic Line), the Awaji region in the northern part of Awaji Island, and the Akashi Strait region where the occurrence of aftershocks was less frequent than in the other two regions. We define a cluster of aftershocks based on the spatial concentration of their locations and common P-axis orientations.

#### 3.1 Kobe region

In the Kobe region (Fig. 5), many aftershocks are observed along the Rokko Fault System (Fig. 1). There are three clusters of aftershocks with strike-slip focal mechanisms near the northeastern end of the Rokko Fault, the Gosukebashi Fault and the Ashiya Fault (area a in Fig. 5). P-axis directions of these aftershocks are approximately horizontal in an ESE-WNW direction.

A cluster of reverse fault type aftershocks exists near the southern end of the Gosukebashi Fault and the Otsuki Fault (area b in Fig. 5). They also have P-axes in approximately horizontal E-W or ESE-WNW directions. The focal depths of these aftershocks are 2–7 km. In contrast, most of strike-slip type in the Kobe region are located deeper than 6–8 km.

In the area from the Suwayama Fault and the Nunobiki Fault to the Suma Fault, aftershocks are mainly of strike-slip type. The majority of the P-axes of these events is in an E-W or ESE-WNW direction. However, those of reverse fault type, located in a cluster along the Suma Fault at depths of

about 12 km, have P-axes in a SE-NW direction, which is almost perpendicular to the strike of the mainshock rupture, as shown in area c of Fig. 5. Most of these events occurred in the second observation period.

#### 3.2 Awaji region

The occurrence of aftershocks is high in the northern half of Awaji Island (Fig. 6). Although surface rupture was observed on the Nojima Fault in the northwestern part of Awaji Island (Nakata *et al.*, 1995; Awata *et al.*, 1996), most of the aftershocks did not occur directly beneath the Nojima Fault, but along the Higashiura Fault and the Kariya Fault, and around the southern end of the Nojima Fault.

We recognize an aggregation of aftershocks around the southern end of the Nojima Fault (area a in Fig. 6). The azimuths of P-axes of these events are approximately in an E-W or ESE-WNW direction, which are the same as those for most aftershocks in the Kobe region. However, the aftershocks in this area are distributed in a wide range of depths, locations, and are of various focal mechanism types. We consider that this aggregation of aftershocks can not be defined as cluster.

There are many aftershocks in the northeastern part of Awaji Island. These events are not in clusters like those in the Kobe region. Their directions of P-axes are also highly variable. Synthetic tests show that this is not caused by the uncertainty of focal mechanism determination. Many reverse fault type events occurred here, compared to those in the Kobe region. Mechanism types of aftershocks do not show any coherent patterns in a small area.

#### 3.3 Akashi Strait

The aftershocks activity in the Akashi Strait (Fig. 7) is extremely low, as reported by Hirata *et al.* (1996) and Nakamura and Ando (1996). Four foreshocks occurred in this area, together with the mainshock. We find two small clusters in this area. One is located at a depth of about 15 km beneath the central part of the Akashi Strait (area a in Fig. 7). The aftershocks in this cluster are mainly of strike-slip type with P-axes rotated clockwise about  $10^\circ$  relative to those of the mainshock and the two foreshocks determined by Katao *et al.* (1997).

The other cluster is located at a depth of about 6 km beneath the eastern part of the Akashi Strait (area b in Fig. 7). Most of the events in this cluster are of reverse fault type. P-axes of these aftershocks are oriented approximately in N-S, in contrast with the regional compressional direction of E-W to ESE-WNW.

#### 3.4 Temporal variation in aftershock mechanisms

The temporal variation in P-axes directions related to a large earthquake was studied by Zhao *et al.* (1997). They reported that the average direction of P-axes in the epicentral area of the 1994 Northridge earthquake changed from  $N30^\circ E$  to  $N13^\circ E$  before and after the mainshock, suggesting the coseismic stress rotation. Furthermore, they showed that the stress orientation rotated back to its original orientation ( $N34^\circ E$ ) during the two years following the mainshock.

Here, we consider whether or not the P-axis directions of aftershocks show any temporal changes for the Hyogo-ken Nanbu earthquake. Because P-axis directions vary widely over the aftershock region (Fig. 5, 6, and 7), we investigate the possibility of a temporal change in P-axis directions sep-

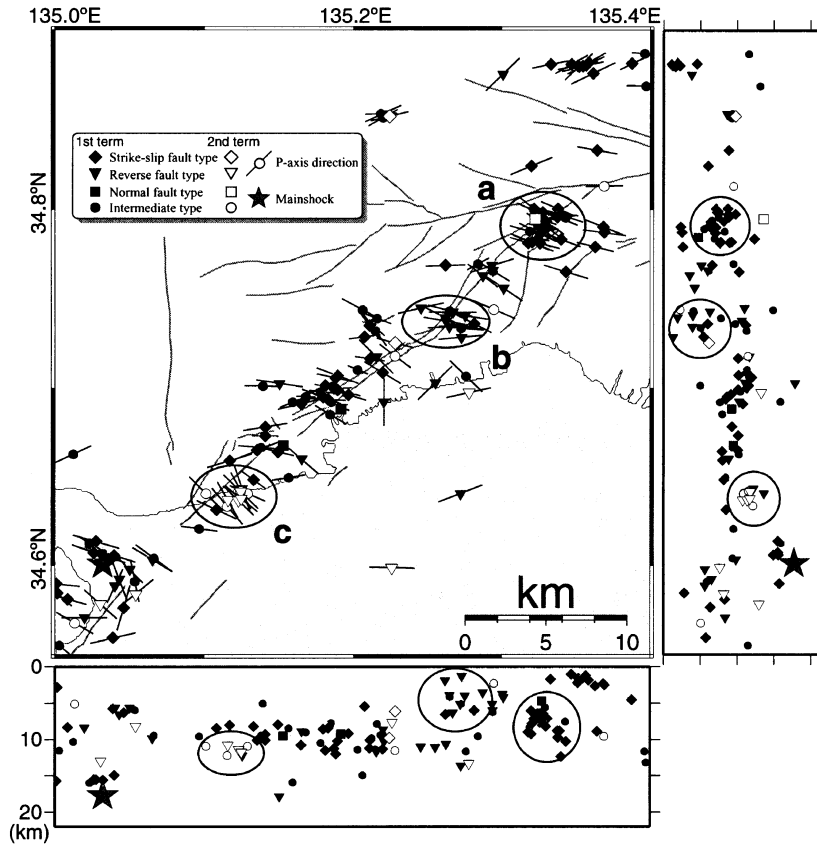


Fig. 5. Type of focal mechanisms of aftershocks in the Kobe region. Diamonds represent strike-slip type, triangles for reverse-fault type and squares for normal-fault type. Circles show intermediate types. Solid and open symbols represent the aftershocks observed in the 1st (from Jan. 26 to May 12, 1995) and 2nd observation periods (from Oct. 1, 1995 to Jan. 12, 1996), respectively. Short bars attached to epicenter circles represent the horizontal projections of P-axes. Star shows the hypocenter of the mainshock.

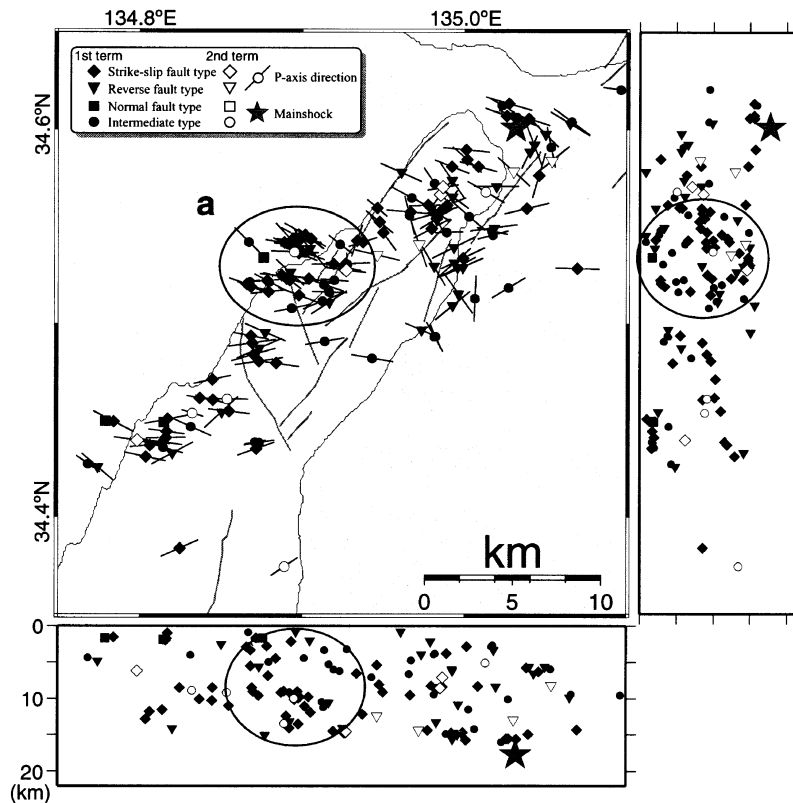


Fig. 6. Type of focal mechanisms of aftershocks in the Awaji region. All symbols are the same as those in Fig. 5.

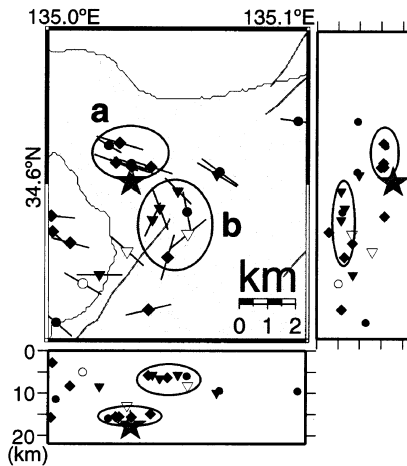


Fig. 7. Type of focal mechanisms of aftershocks in Akashi Strait. All symbols are the same as those in Fig. 5.

arately for each cluster that we identified. We use the focal mechanism solutions from January 17, 1995 to January 28, 1995 determined by Katao *et al.* (1997), in addition to those determined in this study. Within the accuracy of the present data set, we observe no temporal changes in focal mechanism orientations in area c in Fig. 5 from the first to the second period of observation (Fig. 8).

#### 4. Discussion

Most aftershocks ( $M \geq 2.3$ ) have strike-slip or reverse fault mechanisms with P-axes approximately in an E-W or ESE-WNW direction (Fig. 5, 6, and 7). Katao *et al.* (1997) reported that P-axes of many aftershocks are approximately in an E-W direction. They compared their results with the regional stress field in the Kinki District: the E-W compression before the Hyogo-ken Nanbu earthquake reported by Iio (1996). They suggested that the mainshock rupture zone was still controlled by the regional stress field of E-W compression even after the large mainshock. In this study, events with P-axes in E-W directions are observed along the mainshock rupture zone for aftershocks within the clusters of the strike-slip events close to the Rokko Fault and the northern end of the Gosukebashi Fault (area a in Fig. 5), the cluster of reverse fault events near the southern end of the Gosukebashi Fault (area b in Fig. 5) and the aggregation of aftershocks near the southern edge of the Nojima Fault (area a in Fig. 6). We consider that these regions are controlled by the regional stress field of approximately E-W compression after the mainshock.

On the other hand, we observe many aftershocks whose P-axes are inconsistent with the regional stress. A small number of normal mechanism events occurred along the mainshock rupture zone, as Katao *et al.* (1997) pointed out. The aftershocks along the Suma Fault show mainly reverse mechanism solutions with P-axes in a SE-NW direction (area c in Fig. 5). In the eastern part of the Akashi Strait (area b in Fig. 7), the aftershocks with N-S compressional focal mechanism form a cluster. We further detect a large scatter of P-axis directions for the aftershocks in the northeastern part of Awaji Island (Fig. 6). Such a complex pattern of aftershock focal mechanisms was also observed in the case of the 1989

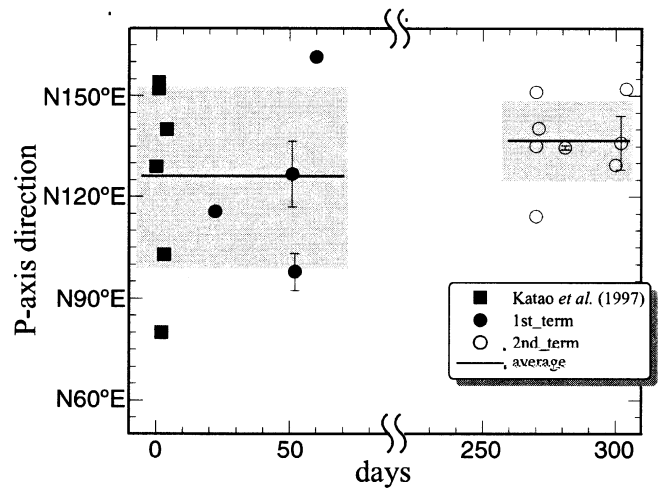


Fig. 8. Temporal variations in P-axis directions for the cluster of aftershocks along the Suma Fault (area c shown in Fig. 5). Solid and open circles represent the P-axis direction of those observed in the 1st and 2nd observation periods, respectively. Solid squares for the first 10 days after the mainshock are data determined by Katao *et al.* (1997). Error bars indicate a range of possible focal solutions.

Loma Prieta earthquake (Michael *et al.*, 1990; Oppenheimer, 1990).

In this study, we call aftershocks that are inconsistent with the regional stress field "atypical." That is, atypical aftershocks are defined as those with a P-axis oriented more than  $45^\circ$  from the E-W direction or with a P-axis plunge of more than  $45^\circ$ . The 48 atypical aftershocks identified in the present data set correspond to about 17% of the total. We compare the spatial distribution of the aftershocks, especially the atypical aftershocks (Fig. 9), with the inverted slip and stress distributions for the mainshock and other parameters to clarify the cause of the occurrence of the atypical aftershocks. The Coulomb stress change by the mainshock was calculated and compared with the induced seismicity rate change in the surrounding areas (Hashimoto, 1997; Toda *et al.* 1998). However, the aftershocks discussed in this study occurred on the mainshock slip plane or very close to it. Because the present precision of hypocenter determination and slip models are not enough to determine whether each aftershock occurs on the hangingwall or footwall side of the mainshock slip plane. It is difficult to explain the atypical focal mechanisms using the Coulomb stress change.

Figure 10 shows a cross section of the hypocenter distribution of the aftershocks relocated in this study with contours of the final stress along the mainshock rupture zone, inferred by Bouchon *et al.* (1998). Bouchon *et al.* (1998) determined the stress and the slip distributions using an inversion technique from strong motion data. In the Kobe region, aftershocks are observed in a belt-like area at depths of about 10 km. Higher final stress is also distributed in the depth range from about 10 km to 15 km. In the Awaji region, aftershocks are observed over a wide depth range, and higher final stress is also distributed widely, in the depth from the surface to 15 km. The distribution of aftershocks corresponds to the areas with higher final stress in the mainshock rupture zone. The shape of the aftershock distribution appears to depend on the degree of the final stress.

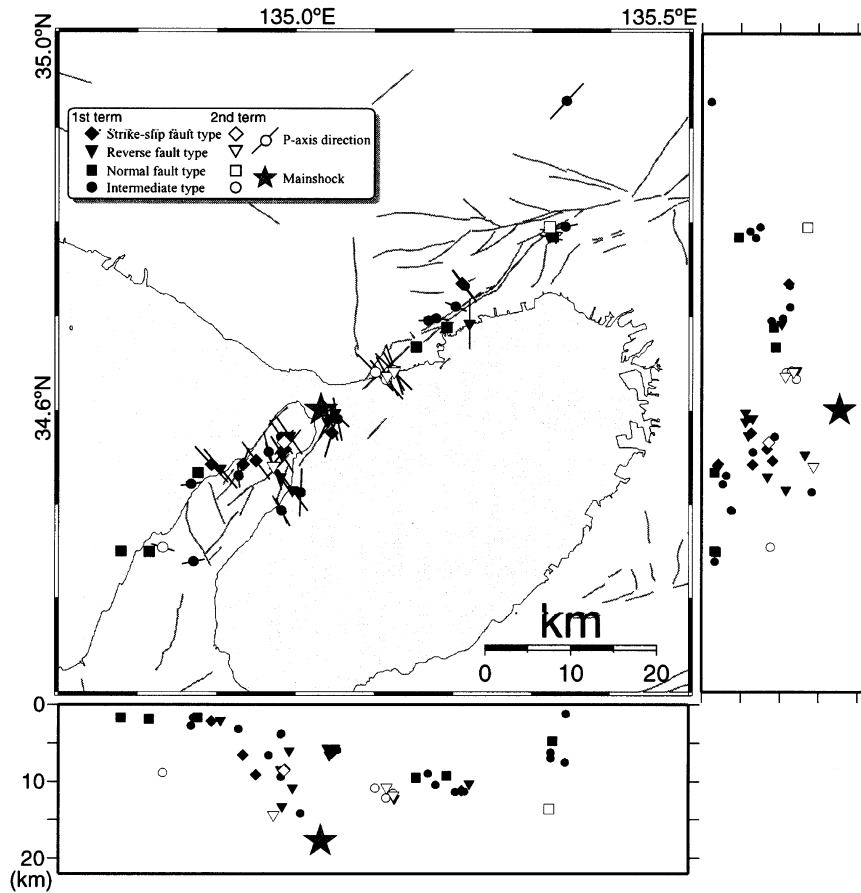


Fig. 9. Distribution of atypical aftershocks with the direction of P-axis inconsistent with the regional stress. All symbols are the same as those in Fig. 5.

Figure 11 shows the locations of the atypical aftershocks and the distribution of the final stress. In the Kobe region, there are atypical aftershocks around the Suwayama Fault and along the Suma Fault (Fig. 9). The atypical aftershocks are located at the boundary between the areas of higher and lower final stress. The locations of the atypical aftershocks are compared with the distribution of the slip for the mainshock shown in Fig. 12. In the Kobe region, the slip of the mainshock is the greatest below about 10 km. For the atypical aftershocks around the Suwayama Fault, especially the events of normal or close to normal fault type near the boundary between the Suwayama Fault and the Suma Fault, we suppose that they are caused by the local stress field perturbed by the difference of displacements at the depth of 10 km. From the comparison with the stress and the slip distributions for the cluster of mainly reverse fault type events observed along the Suma Fault, we can see that these are located on the edge of high stress or large slip area. The focal mechanisms of aftershocks in this cluster are similar to each other (there are two types, reverse and intermediate types, because of the classification of mechanisms), and they are aligned parallel to the active fault at almost the same depths. These are different from other atypical aftershocks distributed in the shallower part of the cluster of strike-slip events in the Kobe region. P-axis directions of these aftershocks are perpendicular to the strike of the active fault (Fig. 9). We consider two possible explanations for this cluster of the atypical aftershocks of mainly reverse fault type

along the Suma Fault. One explanation is that the events are caused by the local stress field disturbed by the heterogeneous displacement near the boundaries of the mainshock rupture. The other is that the shear stress from the regional stress field was adequately canceled by the mainshock slip. Along the San Andreas fault system in central California show the NE-SW compression that is nearly perpendicular to the strike of the fault (Zoback *et al.*, 1987). In the case of this study, however, the regional stress field of E-W compression was observed in a wide area around the rupture faults before/after the mainshock. We consider that the anomalous P-axis directions nearly perpendicular to the strike of the fault are caused by the heterogeneous coseismic slip.

In the Awaji region, there are many atypical aftershocks in the northeastern part of Awaji Island, where P-axis directions of the aftershocks show a large scatter (Fig. 9). The mainshock slip is large in the shallower part of this region. The large slip area extends to a depth of about 15 km (Fig. 12). Around the northern end of Awaji Island, however, there is an area of lower final stress where the mainshock slip was also very small. The atypical aftershocks in the Awaji region are located at this boundary of the rupture following the mainshock slip (in Fig. 12, the aftershocks plotted on the northeastern side of the large slip area, and in Fig. 9, aftershocks located around the Higashiura Fault). The heterogeneity of the mainshock slip altered the local stress field of this area. Moreover, in the northeastern part of Awaji Island, the contour intervals of the slips in the region where atyp-

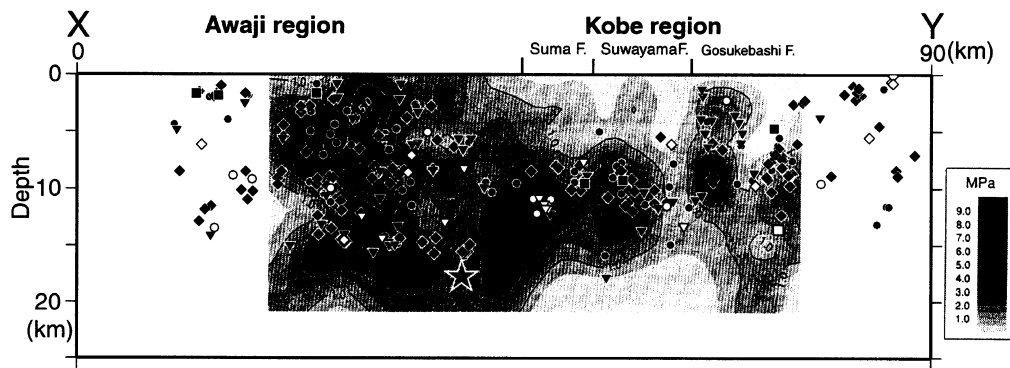


Fig. 10. Cross section of the hypocenter distribution of the aftershocks with the final stress on the mainshock faults of Bouchon *et al.* (1998), along the X-Y line of Fig. 1. All symbols are the same as those in Fig. 5. The contour interval of final stress is 1.0 Mpa.

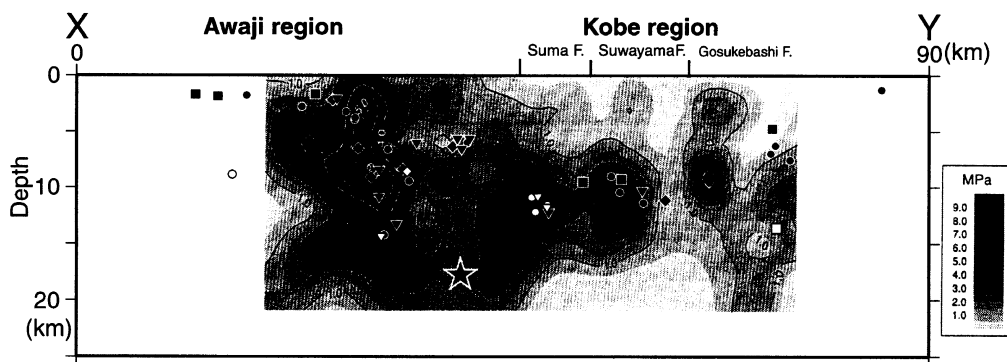


Fig. 11. Cross section of the locations of the atypical aftershocks with the final stress on the mainshock faults of Bouchon *et al.* (1998), along the X-Y line of Fig. 1. All symbols are the same as those in Fig. 5. The contour interval of final stress is 1.0 MPa.

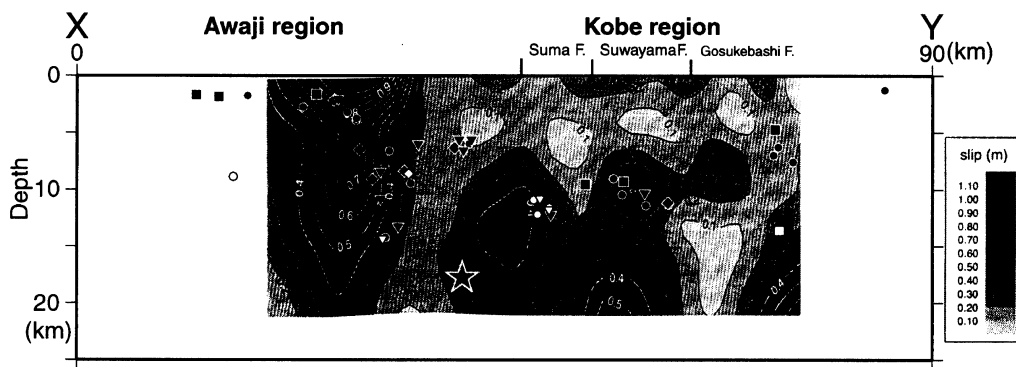


Fig. 12. Cross section of the locations of the atypical aftershocks with the coseismic slip distribution of Bouchon *et al.* (1998), along the X-Y line of Fig. 1. All symbols are the same as those in Fig. 5. The contour interval of slip is 0.1 m.

ical aftershocks occurred are closer than those in the Kobe region, as shown in Fig. 12. That is, the heterogeneity of the mainshock slip is greater on Awaji Island, and the stress field is disturbed to a higher degree, causing atypical aftershocks there.

Tadokoro *et al.* (1999) analyzed S-wave splitting in and around the aftershock region. They showed that the polarization directions of the faster shear wave ( $\psi$ ) in the northern part of Awaji Island were various to strikes of the known active faults. Their results seem to agree with the P-axis directions of the aftershocks determined in this study. For the region where  $\psi$  is not consistent with the regional stress field, the inconsistency appears to be caused by its compli-

cated geology in the northeastern part of Awaji Island. These observations may be partly originated from complicated rupture of the mainshock.

For the cluster of the aftershocks with P-axis in the N-S direction at depths of about 6 km in the eastern part of Akashi Strait (area b in Fig. 7), there is no evidence of the complication in the distribution of the mainshock slip or final stress field. Zhao and Negishi (1998) determined P- and S-wave velocity structures and the distribution of Poisson's ratio in the aftershock region (Fig. 13). There is an area of slow S-wave velocity and high Poisson's ratio in a shallower part of Akashi Strait. This cluster of aftershocks with compressional focal mechanisms might correspond to the boundary

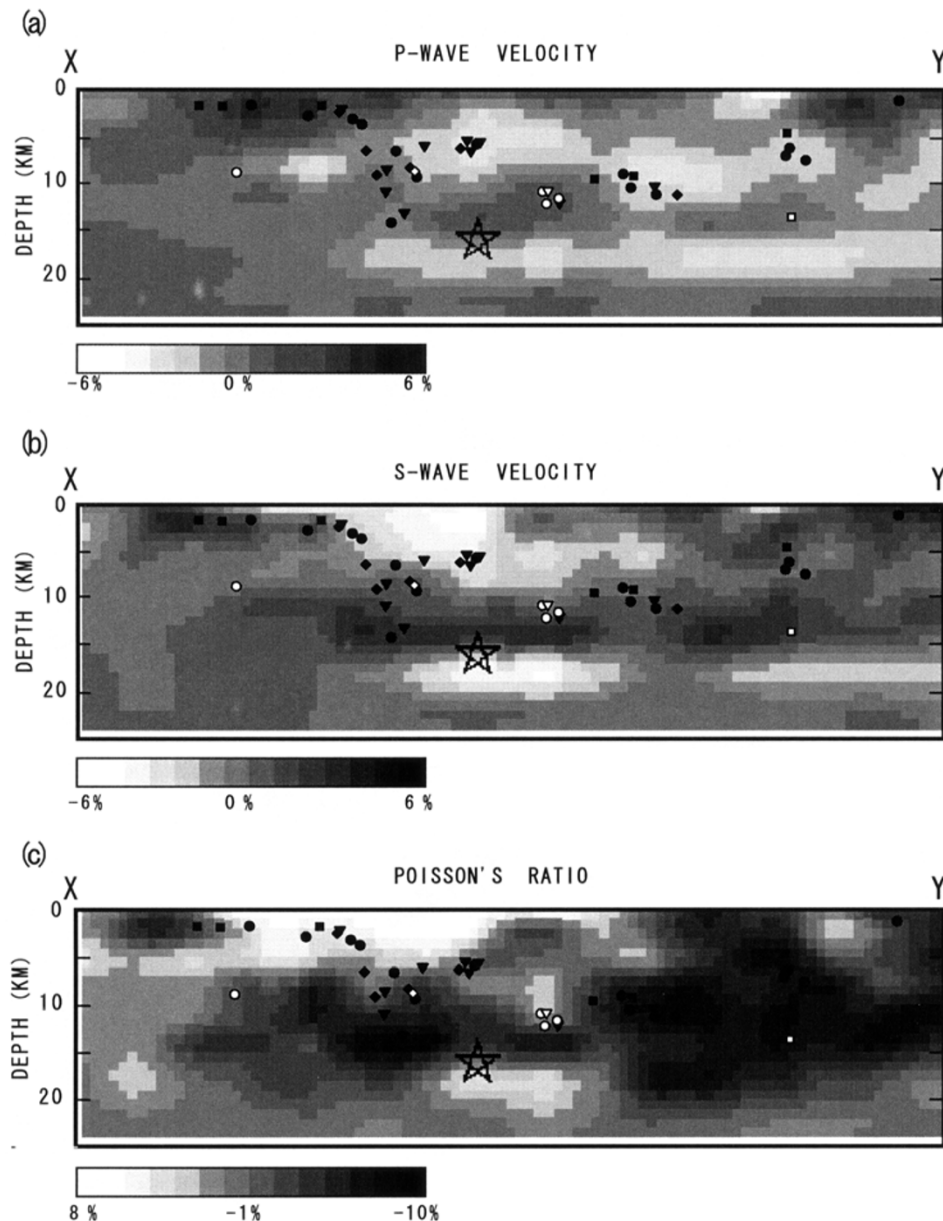


Fig. 13. Cross section of the locations of the atypical aftershocks in comparison with the (A) P-wave velocity, (B) S-wave velocity and (C) Poisson's ratio from Zhao and Negishi (1998), along the X-Y line of Fig. 1. All symbols are the same as those in Fig. 5.

at which S-wave velocity changes rapidly. From the velocity structure of the crust only, however, we cannot surmise the cause of the atypical aftershocks with P-axes in a N-S direction, which is perpendicular to the regional stress field. We cannot detect any obvious corresponding anomaly in P-wave velocity structure. A possible cause of the occurrence of these aftershocks is the geometrical gap in the fault segment beneath the Akashi Strait (Nakamura and Ando, 1996; Takahashi *et al.*, 1996), and the resulting perturbation of the stress field.

## 5. Conclusions

We relocate the hypocenters of the aftershocks of the 1995 Hyogo-ken Nanbu earthquake and determine their focal mechanisms using seismic records obtained by GROUPS-95. The focal mechanisms of the aftershocks are mainly consistent with the regional stress field, which shows E-W

or ESE-WNW compression. However, there are groups of events with different P-axis directions. In the Kobe region, there are clusters of aftershocks which have almost the same direction of P-axes and type of focal mechanisms. In the northeastern part of Awaji Island, P-axis directions of aftershocks are widely spread. In Akashi Strait, there is a cluster of events with N-S compression, almost perpendicular to the regional stress field. We compare the locations of such "atypical" aftershocks with the coseismic slip distribution, the stress distribution after the mainshock, and other geophysical parameters. The atypical aftershocks are mainly located near the boundaries between high and low stress areas, and between slipped and unslipped zones. We suggest that the atypical aftershocks in the mainshock rupture zone are caused by the disturbance of the local stress field due to the heterogeneities of the distributions of the final stress and the mainshock.

**Acknowledgments.** We thank Dapeng Zhao and Hiroaki Negishi for providing their diagram of seismic wave velocity structure. We thank Keiichi Tadokoro for his help to obtain the aftershock data. All participants in GROUPS-95 enable us to do this study. We are grateful to Prof. James Mori and Dr. Peiliang Xu for their careful reading and correction of our manuscript. Comments of Dr. Shigeki Horiuchi, Dr. Kiyoshi Yomogida and an anonymous reviewer are useful to improve our manuscript.

## References

- Aki, K. and P. G. Richards, *Quantitative Seismology*, Vol. 1, W. H. Freeman and Company, New York, 1980.
- Awata, Y., K. Mizuno, Y. Sugiyama, R. Imura, K. Shimokawa, K. Okumura, E. Tsukuda, and K. Kimura, Surface fault ruptures on the northwest coast of Awaji Island associated with the Hyogo-ken Nanbu earthquake of 1995, Japan, *J. Seismol. Soc. Jpn.* 2, **49**, 113–124, 1996 (in Japanese with English abstract).
- Bouchon, M., H. Sekiguchi, K. Irikura, and T. Iwata, Some characteristics of the stress field of the 1995 Hyogo-ken Nanbu (Kobe) earthquake, *J. Geophys. Res.*, **103**(B10), 24271–24282, 1998.
- Hashimoto, M., Correction to “Static stress changes Associated with the Kobe Earthquake: Calculation of changes in Coulomb failure function and comparison with seismicity change”, *J. Seismol. Soc. Jpn.* 2, **50**, 21–27, 1997 (in Japanese with English abstract).
- Hiramatsu, Y., N. Hayashi, M. Furumoto, and H. Katao, Temporal changes in coda  $Q^{-1}$  and  $b$  value due to the static stress change associated with the 1995 Hyogo-ken Nanbu earthquake, *J. Geophys. Res.*, **105**(B3), 6141–6151, 2000.
- Hirata, N. and M. Matsu'ura, Maximum-likelihood estimation of hypocenter with origin time eliminated using nonlinear inversion technique, *Phys. Earth Planet. Inter.*, **47**, 50–61, 1987.
- Hirata, N., S. Ohmi, S. Sakai, K. Katsumata, S. Matsumoto, T. Takanami, A. Yamamoto, T. Iidaka, T. Urabe, M. Sekine, T. Ooida, F. Yamazaki, H. Katao, Y. Umeda, M. Nakamura, N. Seto, T. Matsushima, H. Shimizu, and Japanese University Group of the Urgent Joint Observation for the 1995 Hyogo-ken Nanbu Earthquake, Urgent joint observation of aftershocks of the 1995 Hyogo-ken Nanbu earthquake, *J. Phys. Earth*, **44**, 317–328, 1996.
- Ide, S. and M. Takeo, Determination of constitutive relations of fault slip based on seismic wave analysis, *J. Geophys. Res.*, **102**(B12), 27379–27391, 1997.
- Iio, Y., Depth-dependent change in the focal mechanism of shallow earthquakes: Implications for brittle-plastic transition in a seismogenic region, *J. Geophys. Res.*, **101**(B5), 11209–11216, 1996.
- Katao, H., N. Maeda, Y. Hiramatsu, Y. Iio, and S. Nakao, Detailed mapping of focal mechanisms in/around the 1995 Hyogo-ken Nanbu earthquake rupture zone, *J. Phys. Earth*, **45**, 105–119, 1997.
- Maeda, N., A method of determining focal mechanisms and quantifying the uncertainty of the determining focal mechanisms for microearthquakes, *Bull. Seismol. Soc. Am.*, **82**, 2410–2429, 1992.
- Mendoza, C. and S. H. Hartzell, Aftershock patterns and main shock faulting, *Bull. Seismol. Soc. Am.*, **78**, 1438–1449, 1988.
- Michael, A. J., W. L. Ellsworth, and D. H. Oppenheimer, Coseismic stress changes induced by the 1989 LomaPrieta, California earthquake, *Geophys. Res. Lett.*, **17**, 1441–1444, 1990.
- Nakamura, M. and M. Ando, Aftershock distribution of the January 17, 1995 Hyogo-ken Nanbu earthquake determined by the JHD method, *J. Phys. Earth*, **44**, 329–335, 1996.
- Nakata, T., K. Yomogida, J. Odaka, T. Sakamoto, K. Asahi, and N. Chida, Surface fault ruptures associated with the 1995 Hyogo-ken Nanbu earthquake, *J. Geogr.*, **104**, 127–142, 1995 (in Japanese with English abstract).
- Oppenheimer, D. H., Aftershock slip behavior of the 1989 Loma Prieta, California Earthquake, *Geophys. Res. Lett.*, **17**, 1441–1444, 1990.
- Tadokoro, K., M. Ando, and Y. Umeda, S wave splitting in the aftershock region of the 1995 Hyogo-ken Nanbu earthquake, *J. Geophys. Res.*, **104**(B1), 981–991, 1999.
- Takahashi, N., K. Suyehiro, M. Shinohara, A. Kubo, A. Nishizawa, and H. Matsuoka, Aftershocks and faults of the Hyogo-ken Nanbu earthquake beneath Akashi Strait, *J. Phys. Earth*, **44**, 337–347, 1996.
- Toda, S., R. S. Stein, P. A. Reasenberg, J. H. Dieterich, and A. Toshida, Stress transferred by the 1995 Mw=3.9 Kobe, Japan, shock: Effect on aftershocks and future earthquake probabilities, *J. Geophys. Res.*, **103**(B10), 24543–24565, 1998.
- Urabe, T. and S. Tsukada, A workstation-assisted processing system for waveform data from microearthquake networks, Abstracts of Spring Meeting of Seismological Society of Japan, 70, 1991 (in Japanese).
- Zhao, D. and H. Negishi, The 1995 Kobe earthquake: Seismic image of the source zone and its implications for the rupture nucleation, *J. Geophys. Res.*, **103**(B5), 9967–9986, 1998.
- Zhao, D., H. Kanamori, and D. Wiens, State of stress before and after the 1994 Northridge earthquake, *Geophys. Res. Lett.*, **24**, 519–522, 1997.
- Zoback, M. D., M. L. Zoback, V. S. Mount, J. Suppe, J. P. Eaton, J. H. Healy, D. Oppenheimer, P. Reasenberg, L. Jones, C. B. Raleigh, I. G. Wong, O. Scotti, and C. Wentworth, New evidence on the state of stress of the San Andreas fault system, *Science*, **238**, 1105–1111, 1987.

H. Yamanaka, Y. Hiramatsu, and H. Katao (e-mail: katao@rcep.dpri.kyoto-u.ac.jp)